Biomech Model Mechanobiol
https://doi.org/10.1007/s10237-017-0977-4

ORIGINAL PAPER

Modeling the effect of collagen fibril alignment on ligament mechanical behavior

Christina J. Stender[1] · Evan Rust[1] · Peter T. Martin[1] · Erica E. Neumann[1] · Raquel J. Brown[2] · Trevor J. Lujan[1]

Received: 8 February 2017 / Accepted: 30 October 2017

Abstract Ligament mechanical behavior is primarily regulated by fibrous networks of type I collagen. Although these fibrous networks are typically highly aligned, healthy and injured ligament can also exhibit disorganized collagen architecture. The objective of this study was to determine whether variations in the collagen fibril network between neighboring ligaments can predict observed differences in mechanical behavior. Ligament specimens from two regions of bovine fetlock joints, which either exhibited highly aligned or disorganized collagen fibril networks, were mechanically tested in uniaxial tension. Confocal microscopy and FiberFit software were used to quantify the collagen fibril dispersion and mean fibril orientation in the mechanically tested specimens. These two structural parameters served as inputs into an established hyperelastic constitutive model that accounts for a continuous distribution of planar fibril orientations. The ability of the model to predict differences in the mechanical behavior between neighboring ligaments was tested by (1) curve fitting the model parameters to the stress response of the ligament with highly aligned fibrils and then (2) using this model to predict the stress response of the ligament with disorganized fibrils by only changing the parameter values for fibril dispersion and mean fibril orientation. This study found that when using parameter values for fibril dispersion and mean fibril orientation based on confocal imaging data, the model strongly predicted the average stress response of ligaments with disorganized fibrils ($R^2 = 0.97$); however, the model only successfully predicted the individual stress response of ligaments with disorganized fibrils in half the specimens tested. Model predictions became worse when parameters for fibril dispersion and mean fibril orientation were not based on confocal imaging data. These findings emphasize the importance of collagen fibril alignment in ligament mechanics and help advance a mechanistic understanding of fibrillar networks in healthy and injured ligament.

Keywords Fiber distribution · Constitutive model · Confocal imaging · Hyperelastic · Tensile testing · Transversely isotropic

1 Introduction

Ligament mechanical behavior is governed by the composition and organization of its fibrous protein network. The primary fibrous constituent of ligament is type I collagen, a structural protein that assembles hierarchically from tropocollagen into fibrils, fibers, and then fascicles. Collagen networks in healthy ligament, as well as tendon, typically exhibit uniaxial alignment. However, healthy ligament and tendon can also exhibit disorganized collagen architecture (Clark and Harryman 1992; Gohkle et al. 1994; Provenzano and Vanderby 2006). These disorganized collagen networks are prevalent in granulation tissue and scar tissue, and may be associated with the inferior mechanical properties observed in repaired ligament (Frank et al. 1999). Studying the effect of collagen architecture on ligament mechanical behavior could advance a mechanistic understanding of fibrous networks and clarify the functional impact of microstructural adaptations.

✉ Trevor J. Lujan
trevorlujan@boisestate.edu

[1] Mechanical and Biomedical Engineering, Boise State University, 1910 University Drive, Boise, ID 83725-2085, USA

[2] Biomolecular Research Center, Boise State University, 1910 University Drive, Boise, ID 83725-1511, USA

Published online: 24 November 2017

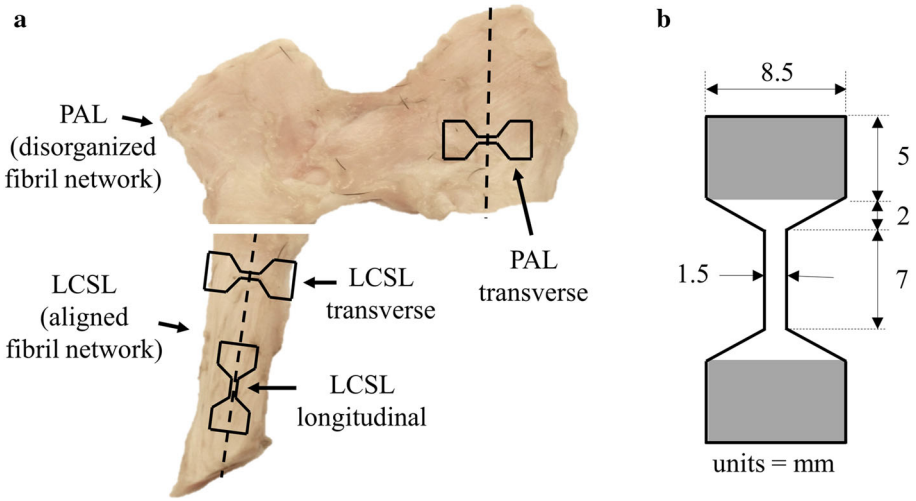

Fig. 1 Specimen acquisition for tensile testing. **a** Specimens were punched longitudinal or transverse to the primary loading axis (as shown by the dashed lines). **b** Punch dimensions, where gray represents the targeted grip region

The mechanical contribution of the collagen network can be examined using constitutive models that incorporate structural parameters into the mathematical stress–strain relationship. These structural parameters can be experimentally measured at variable length scales, and the prediction of mechanical behavior can, therefore, be directly connected to material microstructure. For tissues with disorganized collagen fiber networks, relevant structural parameters include fiber dispersion and mean fiber orientation, which are both properties of the fiber orientation distribution and are measures of material anisotropy. The incorporation of a fiber orientation distribution into constitutive models of soft tissue was introduced by Lanir (1983), and these models have since been used to predict mechanical behavior of the arterial wall (Gasser et al. 2006; Hansen et al. 2009; Holzapfel et al. 2000), aortic valves (Driessen et al. 2005; Freed et al. 2005), pericardium (Sacks 2003), ocular tissue (Girard et al. 2009b), and recently, tendon (Bajuri et al. 2016; Szczesny et al. 2012). However, models that incorporate a fiber orientation distribution have not been commonly applied toward ligament (Wan et al. 2012). Moreover, there are few validation studies that use imaging data to quantify the predictive benefit of including a fiber orientation distribution into structural constitutive models of soft tissue (Ni Annaidh et al. 2012; Sacks 2003; Szczesny et al. 2012).

The objective of this study was to determine whether variations in the collagen fibril network between different ligaments are predictive of observed differences in mechanical behavior.

It is hypothesized that the prediction of ligament mechanical behavior will be improved by using an anisotropic constitutive model that incorporates a specimen-specific distribution of fibril orientations from imaging data compared to a constitutive model that assumes transversely isotropic fibril alignment.

2 Methods

2.1 Overview

A combination of experimental and computational methods was used to test the research hypothesis. Twenty-four healthy ligament specimens from eight adult bovine hooves were mechanically tested in uniaxial tension to characterize quasi-static mechanical behavior. The collagen architecture in the mechanically tested specimens was imaged using confocal microscopy. Images were digitally processed using the software application FiberFit to quantify the fibril dispersion and mean fibril orientation of the collagen network (Morrill et al. 2016). These structural parameters were input as specimen-specific material coefficients in constitutive models of ligament. Experimental deformations were applied to the models to simulate the uniaxial tensile tests previously performed. Finally, statistical analysis assessed if using structural parameter values from imaging data improved the constitutive models ability to predict the observed mechanical behavior.

2.2 Tensile testing

Eight hind left fetlock joints were acquired from a local abattoir and were frozen within 5 h of slaughter. The fetlock joints were allowed to thaw for approximately 1.5 h prior to dissection. The lateral collateral sesamoid ligament (LCSL) and palmar annular ligament (PAL) were removed from each joint. These ligaments were selected because the LCSL exhibits a highly aligned fascicle network and the PAL exhibits a disorganized fascicle network (Fig. 1a). These differences in fascicle organization between the LCSL and PAL were observed from gross examination of the fetlock joint. To obtain a consistent cross-sectional area between specimens, each frozen specimen was mounted onto a vibratome

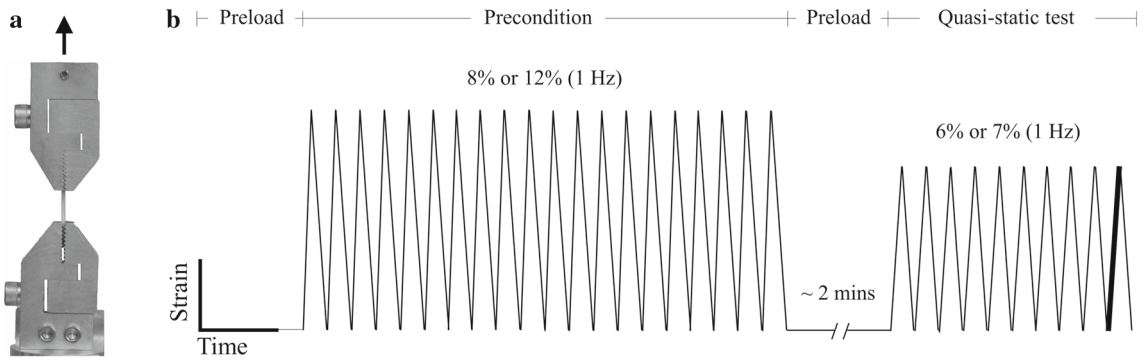

Fig. 2 Mechanical test methods. **a** Specimens were loaded in uniaxial tension. **b** Test protocol (grip-to-grip strain as a function of time), where the applied preload was 0.05 N and the bold portion of the last cycle indicates the region used for mechanical analysis and model validation

Table 1 Physical dimensions of bovine test specimens

Specimen type	Length ± SD	Width ± SD	Thickness ± SD
LCSL longitudinal	11.60 ± 1.23	1.60 ± 0.28	1.93 ± 0.48
LCSL transverse	10.19 ± 1.16	1.51 ± 0.21	1.68 ± 0.36
PAL transverse	11.11 ± 1.31	1.44 ± 0.22	1.80 ± 0.47

grip-to-grip; all units in mm

disk using cyanoacrylate and sliced at a 1.5 mm thickness at a speed of 2.5 mm/s and frequency of 100 Hz (Leica Vibratome VT1000 S, Buffalo Grove, IL). All frozen tissue was then punched into dumbbell-shaped specimens (Fig. 1b) in accordance with the length-to-width aspect ratios recommended in the ASTM standard for testing of fiber-reinforced composite materials in uniaxial tension (ASTM D3039 2004). Specimens from the LCSL were acquired by aligning the long axis of the punch longitudinal or transverse to the preferred orientation of the visible fascicles (Fig. 1a). Specimens from the PAL were acquired by aligning the long axis of the punch transverse to the primary loading axis, which was estimated based on nearby insertion sites. Notably, it was not feasible to punch the PAL specimens relative to the preferred orientation of the fascicles, since the collagen fascicles in the PAL were visibly disorganized and layered. Specimens were clamped for uniaxial tensile tests (Fig. 2a) and loaded into a mechanical test system (Instron E10000, Norwood, MA) with a 10 N load cell (Honeywell, Morristown, NJ; accuracy ± 0.01 N). In total, 24 specimens were tested: eight LCSL longitudinal specimens, eight LCSL transverse specimens, and eight PAL transverse specimens.

Specimens were preconditioned prior to quasi-static mechanical testing. The preconditioning protocol consisted of a 0.05 N preload, followed by 20 triangular cycles at 1 Hz (Fig. 2b). Longitudinal and transverse specimens were preconditioned to 12 and 8% grip-to-grip strain, respectively. This preconditioning protocol was found to improve test repeatability and reduce laxity. Grip-to-grip strain was calculated from a ratio of grip-to-grip displacements ($l/l_o - 1$), where l is the current grip-to-grip displacement and l_o is the reference grip-to-grip displacement (Peloquin et al. 2016; Quapp and Weiss 1998). After preconditioning, a preload of 0.05 N was again applied to establish a consistent reference length. The reference specimen dimensions were quantified by taking the average of three measurements using a digital caliper (Mitutoyo, Aurora, IL; accuracy ± 0.03 mm) (Table 1). Ten triangular cycles at 1 Hz were then applied. Longitudinal specimens were loaded to 7% grip-to-grip strain to ensure the stress–strain response entered a linear region, while transverse specimens were loaded to 6% grip-to-grip strain to avoid tissue damage. Force and displacement were continuously recorded at a sampling frequency of 5 kHz. Cauchy stress along the loading axis was determined from the engineering stress by assuming incompressibility. Mechanical analysis was performed on the first half of the 10th triangular cycle (Fig. 2b). Using a MATLAB linear curve fitting function, 'lsqrcurvefit,' the linear modulus for longitudinal specimens was calculated as the slope of the stress–strain curve when it entered a region with a highly linear correlation ($R^2 \geq 0.98$), and the linear modulus for transverse specimens was calculated as the slope of the last quarter of the stress–strain curve. The transition point on the stress–strain curve between the nonlinear toe region and the linear region was used to compute the transition stress and helped compute the toe region modulus (Lake et al. 2009).

2.3 Confocal imaging

Following cyclic mechanical testing, specimens were removed from the clamps for confocal imaging. Microscopy

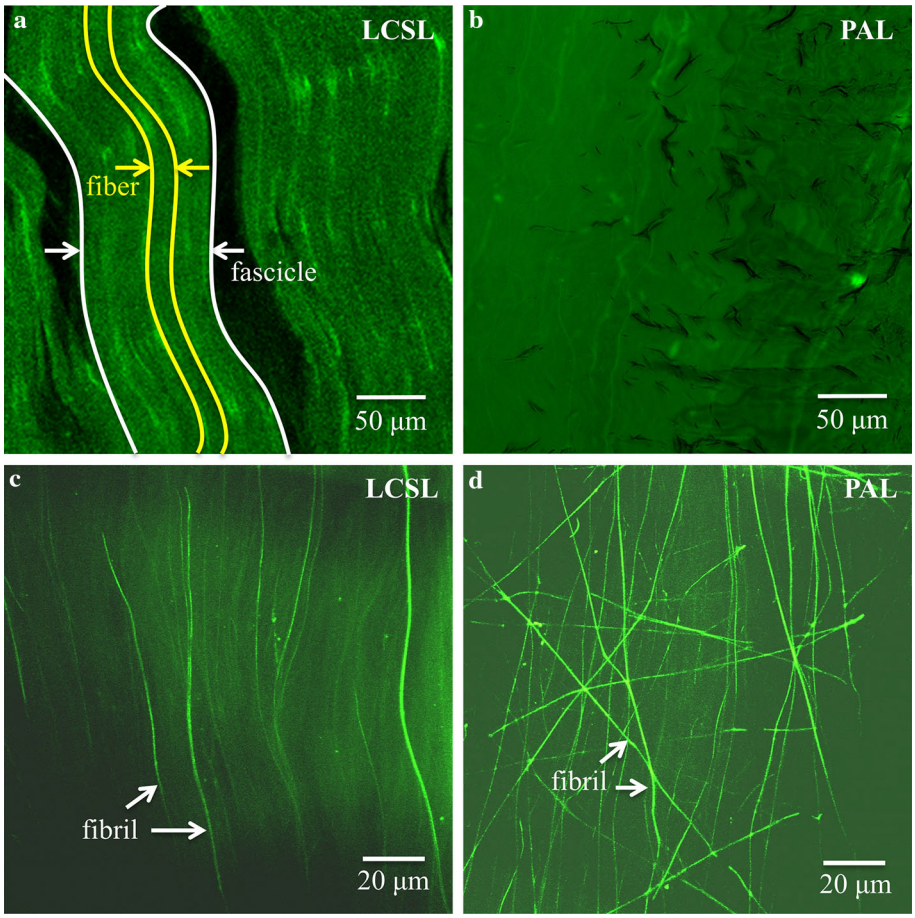

Fig. 3 Confocal images of the LCSL and PAL show differences in collagen organization at different hierarchal levels. **a** Collagen fascicles and fibers could be distinguished in the LCSL, **b** but were difficult to distinguish in the PAL. **c** Collagen fibrils are highly aligned in the LCSL, **d** and are disorganized in the PAL. All confocal images analyzed for this study were acquired using a 63× objective lens to view the fibril network as distinct elongated structures (**c** and **d**)

slides were prepared by embedding the entire dumbbell specimens in cryogel and slicing to a thickness of 50 μm using a cryostat at − 20°C (Leica CM1950 Cryostat, Buffalo Grove, IL). Prior to embedding the specimens in cryogel, hemostats were used to manually stretch the specimens to approximately the maximum strain applied during quasi-static testing in order to image the collagen networks in the linear stress–strain region. The autofluorescence of collagen fibrils and elastin was imaged with a Zeiss LSM 510 Meta system combined with the Zeiss Axiovert Observer microscope and ZEN 2009 imaging software (Carl Zeiss, Inc., Thornwood, NY). By using confocal microscopy (Fig. 3a–d), collagen fibrils in the LCSL and PAL can be viewed as distinct elongated structures (Fig. 3c–d). Imaging data were acquired with a Diode laser source (405 nm), a 63× Plan-Apochromat oil-immersion objective lens (numerical aperture = 1.4) and an emission long pass filter of 505 nm (Monici 2005). Multiple images from overlapping optical sections (2 μm) were collected in a z-stack, projected into a 2-D image and exported for analysis. Three z-stack projections, 2 μm deep, from three distinct regions near the center of the gauge length were obtained from each LCSL longitudinal specimen and from each PAL transverse specimen. Using the scale bar and zoom features within the ZEN imaging software, a random sampling of collagen diameters was used to verify that θ_p and k were being analyzed from images of collagen fibrils, and not collagen fibers. The collagen fibril diameters in this study were between 300 and 1000 nm, while the reported range for collagen fibrils in rat tail tendon is between 50 and 500 nm (Kastelic et al. 1978; Screen et al. 2004).

Each LCSL transverse specimen was assumed to exhibit the same collagen fibril network as the LCSL longitudinal specimen that was punched from the same fetlock joint. In total, 48 z-stacks were acquired. The collagen fibril network was visible in all z-stacks, except for five z-stacks from two LCSL specimens. To approximate the LCSL collagen network in these two specimens, five z-stacks were acquired in the contralateral LCSL. These contralateral specimens underwent the same freezing protocol, but were not subjected to uniaxial tensile testing. A potential reason that fibrils could not be clearly imaged in five of the LCSL z-stacks is that high tissue density limited the depth of laser penetration.

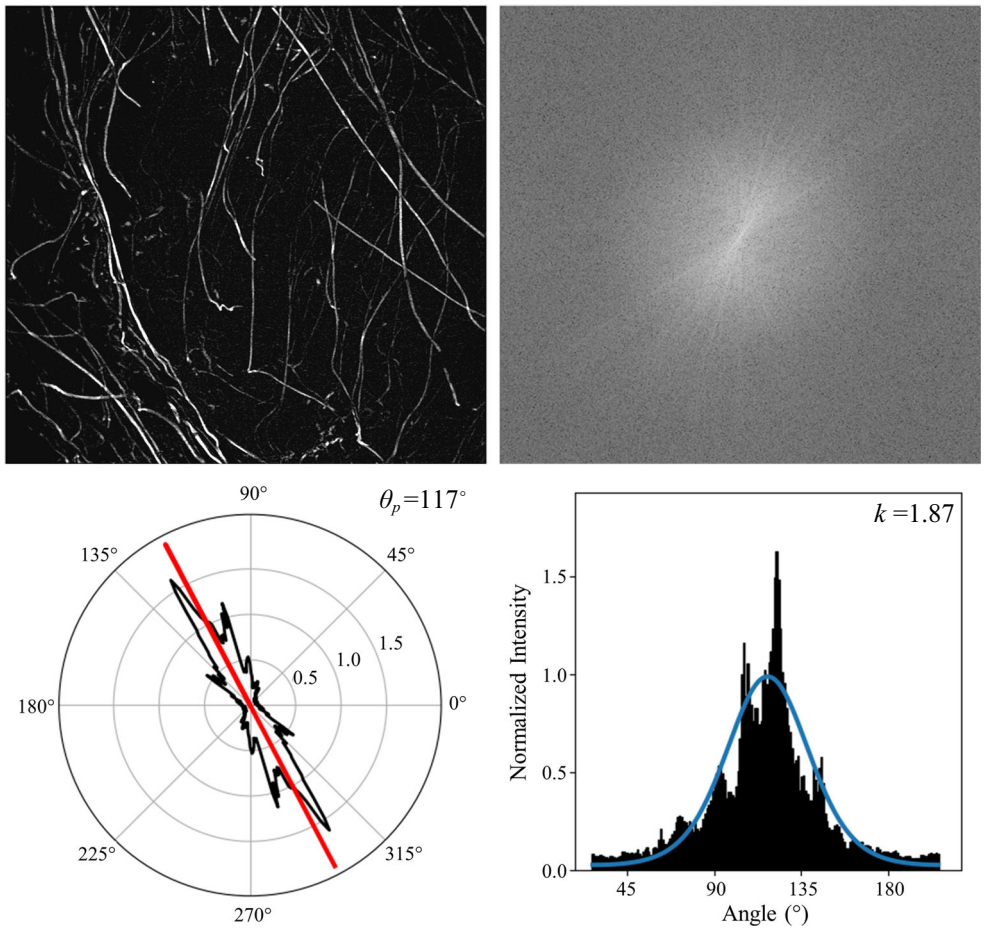

Fig. 4 Screenshot of FiberFit user interface after analysis of one confocal image. Upper Left) Grayscale z-stack projection of ligament. Upper Right) Fast Fourier transform power spectrum. Lower Left) Polar plot of normalized power intensity that plots the mean fibril orientation θ_p (red line) using an elliptical best fit. Lower Right) Cartesian plot of the normalized power intensity with the best-fit semicircular von Mises distribution (blue curve) to calculate the fibril dispersion k

2.4 Image processing

The collagen fibril network in each z-stack projection was analyzed using FiberFit (Morrill et al. 2016), a free software application that utilizes a fast Fourier transform (FFT) and a semicircular von Mises distribution to estimate mean fibril orientation, θ_p, and fibril dispersion, k.The parameter k is analogous to the reciprocal of variance, where an increase in k signifies alignment of fibrils toward the mean fibril orientation, θ_p. A k of zero signifies no mean fibril orientation (i.e., isotropic), and a k above 10 represents a nearly transversely isotropic material that exhibits a highly aligned fibril network. A θ_p of zero signifies that the mean fibril orientation is aligned with the loading direction during uniaxial tensile testing. The physical alignment of the imaged data with the experimental loading direction was accomplished by first aligning the long axis of the dumbbell-shaped specimens with the long axis of the glass slides when slicing the specimens in the cryostat; and then using a protractor to estimate any deviations between the long axes of the specimen and glass slide, and rotating the confocal images to account for this deviation. Prior to processing in FiberFit, the brightness and contrast of each grayscale confocal image was adjusted to reduce noise and enhance the appearance of the collagen fibrils. For the 48 z-stack projections analyzed using FiberFit (Fig. 4), the average coefficient of correlation (R^2) between the semicircular von Mises distribution and the fibril orientation histogram was 0.72 ± 0.17. After FiberFit analysis, the microstructural parameters, k and θ_p, were quantified from the three z-stack projections of each imaged specimen and were averaged and inputted into the constitutive models. For θ_p, the average value for each imaged specimen was calculated using the circular mean (Mardia and Jupp 2000).

2.5 Constitutive models

To determine whether mean fibril orientation θ_p and fibril dispersion k are predictive of ligament mechanical behavior, these microstructural parameters were input into a constitutive model that incorporated a planar distribution of fibril orientations—the *fiber distribution model*. Predictions from the fiber distribution model were compared to a constitutive model that assumed an aligned fibril orientation—the *transversely isotropic model*. In this study, the 'fiber' networks that are being modeled will represent the 'fibril' networks that were measured from the confocal images.

2.5.1 Fiber distribution model

The structural parameters θ_p and k were embedded into an uncoupled hyperelastic strain energy formulation that uses a von Mises distribution of fiber orientations (Girard et al. 2009b). This formulation uses a strain energy term W that accounts for the energy stored in the ground substance and a planar fiber network:

$$W = W_{gs} + \int_{\theta_p-\pi/2}^{\theta_p+\pi/2} P\left(\theta, \theta_p, k\right) W_{\text{fiber}}\left[I_4\left(\theta\right)\right] d\theta \tag{1}$$

Here W_{gs} is the strain energy density of the ground substance using a Mooney–Rivlin model, which has two material coefficients c_1 and c_2 (Mooney 1940; Rivlin 1948); and W_{fiber} is the strain energy density of the fibrous network that uses a previously described piecewise function (Gardiner and Weiss 2003; Weiss et al. 1996), which has four unique material coefficients, $c_3 - c_5$ and λ^*. The domain intervals in this piecewise function are determined by λ^*, which represents the stretch when collagen straightens from a crimped state (i.e., transition strain). In this study, W_{fiber} will physically represent the collagen fibril network in ligament. The integral term accounts for the energy stored in a normal distribution of fibers, where P is the semicircular von Mises distribution:

$$P\left(\theta, \theta_p, k\right) = \frac{1}{\pi I_o\left(k\right)} e^{k\cos\left(2\left(\theta-\theta_p\right)\right)} \tag{2}$$

The I_o term is the modified zero-order Bessel function:

$$I_o\left(k\right) = \frac{1}{\pi} \int_0^{\pi} e^{k\cos(x)} dx \tag{3}$$

Note that P is a normal distribution and satisfies the normalization condition:

$$\int_{\theta_p-\pi/2}^{\theta_p+\pi/2} P\left(\theta, \theta_p, k\right) d\theta = 1 \tag{4}$$

The 2nd Piola–Kirchhoff stress $\mathbf{S}$ can be calculated from the dilational and deviatoric strain energy density, W_{vol} and $\tilde{W}$, respectively, using scalar invariants of the right Cauchy–Green deformation tensor $\mathbf{C}$, which is calculated from the deformation gradient tensor $\mathbf{F}$ ($\mathbf{C} = \mathbf{F}^T \cdot \mathbf{F}$):

$$\mathbf{S} = 2\left(\frac{\partial W_{vol}\left(J\right)}{\partial \mathbf{C}} + \frac{\partial \tilde{W}_{gs}}{\partial \tilde{I}_1} \cdot \frac{\partial \tilde{I}_1}{\partial \tilde{\mathbf{C}}} + \frac{\partial \tilde{W}_{gs}}{\partial \tilde{I}_2} \cdot \frac{\partial \tilde{I}_2}{\partial \tilde{\mathbf{C}}} + \frac{\partial \tilde{W}_{fiber}}{\partial \lambda} \cdot \frac{\partial \lambda}{\partial \tilde{I}_4} \cdot \frac{\partial \tilde{I}_4}{\partial \tilde{\mathbf{C}}}\right) \tag{5}$$

Here J is the Jacobian and equals unity when assuming incompressibility, $\tilde{I}_1$ and $\tilde{I}_2$ are the first and second scalar invariants of $\tilde{\mathbf{C}}$, which is the uncoupled deviatoric right Cauchy–Green deformation tensor, and $\tilde{I}_4$ is defined as:

$$\tilde{I}_4\left(\theta\right) = \mathbf{a}_0\left(\theta\right) \cdot \tilde{\mathbf{C}} \cdot \mathbf{a}_0\left(\theta\right) = \lambda^2 \tag{6}$$

where $\boldsymbol{a}_o$ is a unit vector that represents the local fiber orientation prior to deformation and λ is the fiber stretch. The 2nd Piola–Kirchhoff stress $\mathbf{S}$ is converted to Cauchy stress, $\mathbf{T}$, using a push forward operation:

$$\mathbf{T} = p\mathbf{I} + \frac{2}{J}\left[c_1\left(\tilde{\mathbf{B}} - \frac{1}{3}\tilde{I}_1\mathbf{I}\right) + c_2\left(\left(\tilde{I}_1\tilde{\mathbf{B}} - \tilde{\mathbf{B}}^2\right) - \frac{2}{3}\tilde{I}_2\left(\theta\right)\mathbf{I}\right)\right] + \int_{\theta_p-\pi/2}^{\theta_p+\pi/2} P\left(\theta, \theta_p, k\right) \frac{\lambda\tilde{W}_{\lambda}}{J}\left(\mathbf{a}\otimes\mathbf{a} - \frac{1}{3}\mathbf{I}\right) d\theta \tag{7}$$

where $\tilde{W}_{\lambda}$ is the partial derivative of $\tilde{W}_{\text{fiber}}$ with respect to λ, p is the hydrostatic pressure, and $\mathbf{a}$ is a unit vector that represents the local fiber orientation after deformation. The Cauchy stress values predicted by the model along the axis of loading (T_{11}) can be directly compared to the Cauchy stress values that were experimentally calculated from the uniaxial tensile tests.

2.5.2 Transversely isotropic model

A common transversely isotropic fiber model for ligament is a hyperelastic formulation developed by Weiss et al. (1996). This transversely isotropic model uses the same W_{gs} and W_{fiber} described previously for the fiber distribution model [Eq. 1]. By using a very large k value in the fiber distribution model [Eq. 7], the fibers become highly aligned, and the fiber distribution model effectively reduces to the transversely hyperelastic model developed by Weiss et al. (Fig. 5). For this study, a transversely isotropic model was created by inserting a large k value of 500 in the fiber distribution formulation.

2.6 MATLAB implementation

The fiber distribution model from Sect. 2.5.1 was implemented into MATLAB. Incremental deformations were prescribed to a unit cube based on the unidirectional strain applied during tensile experiments. Volume preservation was assumed (i.e., isochoric deformation), and the hydrostatic pressure term p (Eq. 7) was calculated by setting the in-plane stress component, normal to the loading direction, to zero. For the fiber distribution model, the integral was approximated numerically by utilizing 181 equally divided angles between $\theta_p - \pi/2$ and $\theta_p + \pi/2$. The three-dimensional Cauchy stress tensor $\mathbf{T}$ and engineering strain tensor $\mathbf{E}$ ($\mathbf{E} = \mathbf{U} - \mathbf{I}$, where $\mathbf{U}$ is the right stretch tensor) were calculated, and plots were generated for the stress and strain components along the direction of loading. Please note that the strain $\mathbf{E}$ used in this study is also called Biot strain.

The MATLAB model was verified using the open source finite element modeling software FEBio (Maas et al. 2012). The 'Mooney–Rivlin von Mises Fibers' model in FEBio, which uses the same constitutive equations as the fiber distribution model implemented in MATLAB (Eq. 7), was selected for a single 8-node hexahedral element. The element was loaded to a stretch of 1.1 along the mean fiber orientation ($\theta_p = 0$) using k values of 0.5, 1, and 5, while all other material coefficients were kept constant (bulk modulus $= K = 100,000$ MPa, $c_1 = 2.4$ MPa, $c_2 = 0$ Pa, $c_3 = 2.33$ KPa, $c_4 = 25.28$, $c_5 = 253.7$ MPa, $\lambda^* = 1.06$). In FEBio, the hydrostatic pressure term p for the 'Mooney–Rivlin von Mises Fibers' model is a function of bulk modulus, $p = 0.5K\,(\ln J)^2$, and by selecting a large bulk modulus value, a nearly incompressible material can be modeled. By setting $c_2 = 0$, we modeled the isotropic matrix as a neo-Hookean solid. The FEBio results were compared to the results from the MATLAB fiber distribution model using the same material coefficients (Fig. 5). To test the validity of the transversely isotropic fiber model described in Sect. 2.5.2, the 'trans iso' model in FEBio was selected for the single 8-node element. Results from the trans iso FEBio model were compared to the MATLAB fiber distribution model with a k value of 500 (all other coefficients were equal between the MATLAB and FEBio models). A very strong positive correlation existed between MATLAB and FEBio for all comparisons ($R^2 = 1.00$) (Fig. 5). This excellent correlation verified that the fiber distribution model and the transversely isotropic model used in this study had been correctly implemented into MATLAB.

2.7 Parameter estimation and model validation

To test the study hypothesis, a model validation strategy was developed with two stages (Fig. 6). In stage one, the six nonstructural material coefficients, c_1–c_5 and λ^*, in the fiber distribution model (see 2.5.1) were curve fit to the LCSL experimental stress–strain results (longitudinal and transverse). All curve fits for c_1–c_5 were automatically generated in MATLAB using the nonlinear least-squares algorithm 'lsqrcurvefit' to minimize the sum of squares difference between the experimental and theoretical stress values. Initial guesses were constrained to positive real numbers, except for c_2, which was unconstrained. In stage two, these six material coefficients were held constant to determine if specimen-specific differences in the PAL fibril architecture could predict the differences observed in the mechanical behavior between the LCSL and PAL specimens. This two-stage strategy for model validation follows established methods of first curve fitting model parameters to experimental data, and then using an independent data set to test the model predictions. For this study, we curve fit the LCSL mechanical data (stage one) and the PAL mechanical data served as the independent data set to test model predictions (stage two).

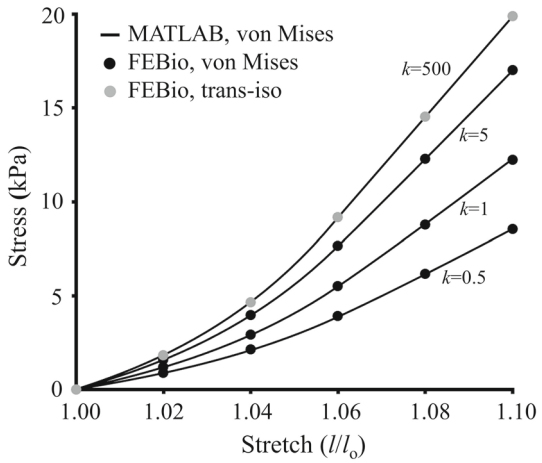

Fig. 5 Comparison of results from the von Mises fiber distribution model implemented in MATLAB, and results from FEBio using similar models and material parameters

Stage one used an iterative and automated procedure to curve fit model parameters to the LCSL experimental data. Although some similarity exists between this procedure and an established curve fitting method for the transversely isotropic model (Quapp and Weiss 1998), fitting the fiber distribution model is notably more complicated since a continuous distribution of fibers will actively resist deformation during both longitudinal and transverse loading. Therefore, we could not use the previously established approach of first fitting c_1 and c_2 to the transverse data, and then fitting c_3–c_5 to the longitudinal data (Quapp and Weiss 1998), and instead we used the following five step iterative approach. In step 1, the λ^* term was calculated by finding the strain value where the LCSL longitudinal stress–strain curve entered a region with a highly linear correlation ($R^2 \geq 0.98$). In step 2, c_1 and c_2 were fit to the LCSL transverse experimental data with the assumption that the deformation was only

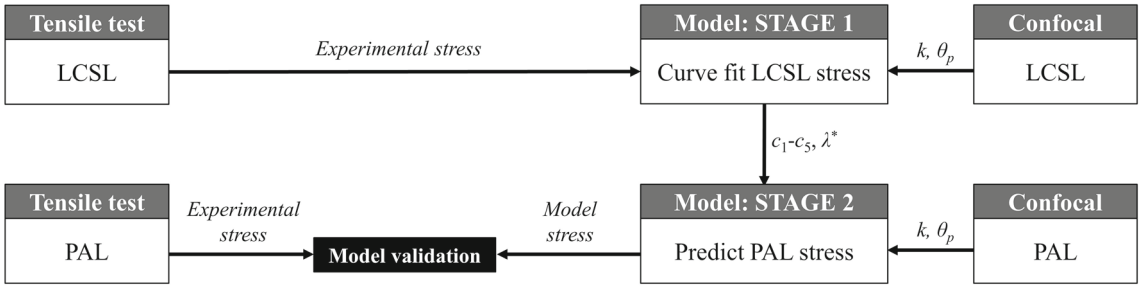

Fig. 6 Two-stage strategy to curve fit and predict experimental results. In stage 1, all model parameters were curve fit to the LCSL experimental stress response. In stage 2, the model was used to predict PAL stress by only updating the structural parameters (k, θ_p) based on specimen-specific confocal imaging of the PAL, while all non-structural parameters, $c1 - c5$ and λ^*, were kept constant. This strategy tested whether differences in mechanical behavior between the LCSL and PAL could be predicted by only adjusting for differences in collagen microstructure between the LCSL and PAL. This two-stage analysis was performed for eight pairs of LCSL and PAL ligaments

resisted by the ground substance, and not the fiber network ($c_3 = c_4 = c_5 = 0$). In step 3, the c_3 and c_4 coefficients were fit to the toe region of the LCSL longitudinal experimental data and c_5 was fit to the linear region of the LCSL longitudinal experimental data, while c_1 and c_2 were taken from step 2. In step 4, c_1 and c_2 were recalculated by fitting them to a modified version of the transverse experimental data. This modified version removed the stress contribution from the fiber network by subtracting the stress response associated with the fiber coefficients, $c_3{-}c_4$, from the transverse experimental data. This effectively allowed the combined stress contribution of the ground substance and fiber network to nicely fit the unmodified transverse experimental data. For this modified version, a boundary condition was enforced that the ground substance could not have a negative stress contribution. In step 5, $c_3{-}c_5$ were refit to the longitudinal experimental data using c_1 and c_2 from step 4. Importantly, the k and θ_p parameters from confocal imaging were used in steps 3–5. This automated methodology was able to produce excellent fits to the experimental data (Fig. 7).

Stage two determined if the model developed in stage one could predict the PAL stress response when only modifying the values of the structural parameters. For this stage, the six non-structural parameters acquired in stage one ($c_1{-}c_5$ and λ^*) were held constant, while the two structural parameters acquired in stage one from confocal imaging of the LCSL (k and θ_p) were substituted with the structural parameters acquired from confocal imaging of the PAL. The PAL model predictions of the stress response were then compared to the actual PAL experimental results for purposes of validation (Fig. 6). We therefore never curve fit the PAL experimental results, but rather tried to predict the PAL experimental results by using values for the structural parameters based on specimen-specific imaging data.

2.8 Sensitivity analysis

To better understand the sensitivity of the PAL model predictions to the structural parameters measured from confocal

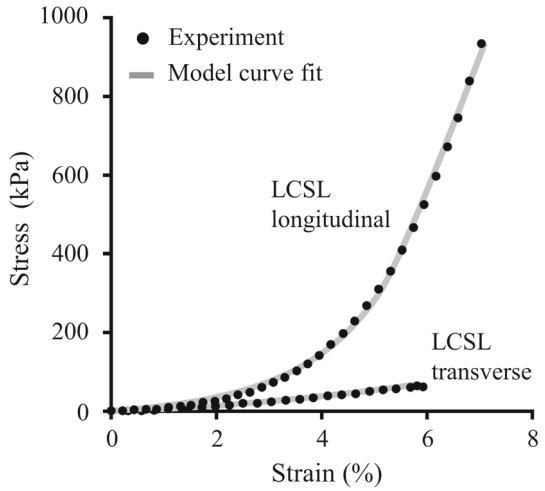

Fig. 7 Curve fitting the material coefficients of the fiber distribution model to the raw data from one representative set of LCSL tensile experiments

imaging, the two-stage validation strategy was performed using four cases of structural parameters. Case 1 was a transversely isotropic model, $k = 500$, with θ_p aligned with the loading direction (this model uses no structural parameter values measured from confocal imaging). Case 2 was a transversely isotropic model, $k = 500$, with θ_p measured from confocal images of the fibril network. Case 3 was a fiber distribution model with θ_p aligned with the loading direction and k measured from confocal images of the fibril network. Case 4 was a fiber distribution model with θ_p and k measured from confocal images of the fibril network. It is important to note that the curve fitting approach described in stage one, to best fit $c_1{-}c_5$ to the specimen-specific LCSL experiments, was independently repeated for each of these four cases. For example, to apply case 3, we would curve fit the LCSL data using only one specimen-specific structural parameter (k), and θ_p would be aligned along the loading direction. Then when predicting the PAL stress response, we would only adjust one specimen-specific parameter (k), and

θ_p would again be aligned along the loading direction. This strategy resulted in different model parameters for each case and allowed us to determine what specimen-specific structural parameters were most beneficial for predicting changes in the mechanical response of ligament.

2.9 Statistical analysis

Statistical analysis was performed in multiple parts using SPSS (Version 23; IBM Corp., Armonk, NY). The effect of specimen harvest location on the experimental linear modulus, peak stress, θ_p, and k was assessed using MANOVA. A MANOVA also assessed the ability of the constitutive models to predict PAL linear modulus and peak stress, and was used to measure the effect of model type on the material coefficients selected to best fit the LCSL experimental results. For all MANOVA tests, an LSD post hoc test was used for equal variances, and a Games–Howell test for unequal variances. The quality of the model fits to the LCSL and PAL stress–strain behavior was quantified using the Nash–Sutcliffe efficiency coefficient (R^2). Significance was set to $p < 0.05$, and all results were reported with standard deviation.

3 Results

3.1 Tensile testing

The LCSL longitudinal, LCSL transverse, and PAL transverse specimens exhibited unique stress–strain behavior under tensile loading (Fig. 8). Compared to the LCSL transverse specimens, the PAL transverse specimens had a nearly four times greater linear modulus ($p < 0.01$) and a three times greater peak stress ($p < 0.01$); while compared to the LCSL longitudinal specimens, the PAL transverse specimens had one-fifth of the linear modulus ($p < 0.01$) and one-third of the peak stress at 6% grip-to-grip strain ($p < 0.01$) (Table 2).

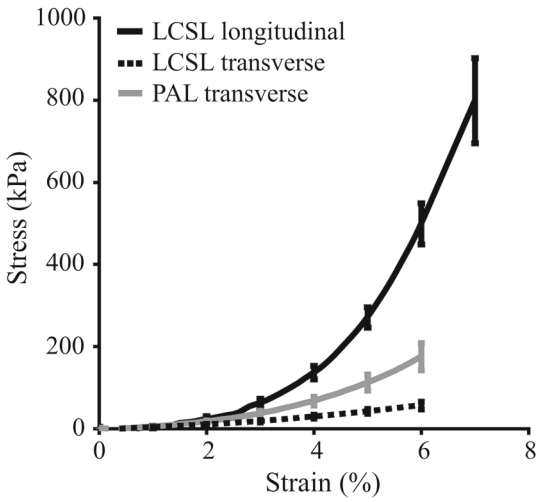

Fig. 8 Average stress–strain response of tensile experiments performed on LCSL and PAL specimens, when loaded longitudinal or transverse to the primary direction of the visible fascicles

3.2 Imaging

The mean fibril orientation θ_p for the LCSL longitudinal specimens was nearly aligned to the loading axis, and for the LCSL transverse specimens was nearly perpendicular to the loading axis (Table 2). The mean fibril orientation θ_p for the PAL transverse specimens was close to perpendicular to the loading axis (Table 2). The fibril dispersion k for the PAL transverse specimens was nearly one-fifth the value of the LCSL specimens, indicating that the PAL had a more disorganized fibrillar structure than the LCSL, but this difference was not significant ($p = 0.057$). The average intra-specimen variability in measuring fibril dispersion from confocal images for LCSL longitudinal and PAL transverse specimens was 1.5 and 0.7, respectively. The average intra-specimen variability in measuring mean fibril orientation from confocal images for LCSL longitudinal and PAL transverse specimens was 7.6 and 34.7 deg, respectively.

3.3 Parameter estimation

The automated curve fitting approach used to fit model parameters to each longitudinal and transverse LCSL experiment resulted in average stress–strain curves with very strong positive correlations to the average LCSL experimental data ($R^2 = 1.0$; Fig. 9). These strong correlations occurred when using zero, one, or two structural parameters from confocal imaging data (Table 3). For each individual longitudinal and transverse LCSL experiment, all models had fits with R^2 values greater than 0.93, except for one LCSL transverse specimen that fit poorly to the fiber distribution model ($R^2 = 0.49$; Table 3). No significant differences existed between the fitted coefficients used for the transversely isotropic and fiber distribution models (Table 3).

3.4 Model predictions and sensitivity analysis

The six material coefficients curve fit to each specimen using the LCSL experimental data ($c_1 - c_5$, λ^*; Table 3) were then held constant to determine if differences between the LCSL and PAL structural parameters (k and θ_p) could predict the differences observed in the mechanical behavior between the LCSL and PAL specimens (Fig. 8). The average model results and average PAL experimental results had a very weak relationship when structural parameter values were not based on confocal imaging ($R^2 = 0.12$; Fig. 10a), had a moder-

Table 2 Mechanical Properties and Structural Parameters of Bovine Ligament

Specimen type	Toe region modulus (MPa)	Linear region modulus (MPa)	Transition stress (kPa)	Peak stress (kPa)†	Mean fibril orientation θ_p (deg)	Fibril dispersion k
LCSL longitudinal	5.2 ± 1.3	27.6 ± 12.5	302.3 ± 135.5	536.2 ± 110.0	1.3 ± 9.6	5.7 ± 5.3
LCSL transverse	0.7 ± 0.2[a]	1.5 ± 0.4[a]	31.5 ± 9.1[a]	50.9 ± 15.0[a]	88.7 ± 9.6	5.7 ± 5.3
PAL transverse	1.7 ± 0.6[a]	5.6 ± 2.5[a]	80.9 ± 28.2[a]	157.9 ± 60.1[a,b]	78.9 ± 39.3	1.1 ± 0.8

†Calculated at 6% grip-to-grip strain
[a] Significantly different than LCSL longitudinal data ($p \leq 0.05$)
[b] Significantly different than LCSL transverse data ($p \leq 0.05$)

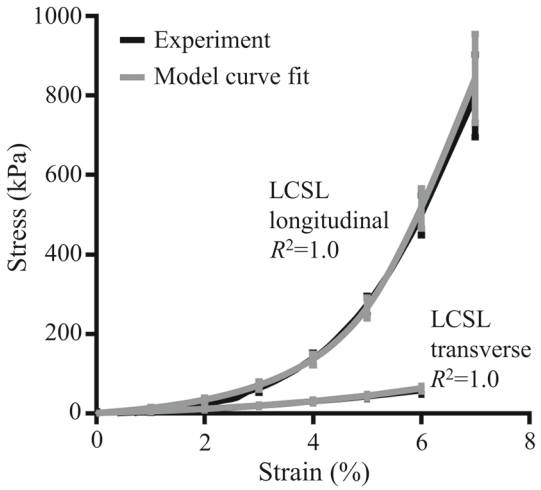

Fig. 9 By using an automated curve fitting approach to select $c_1 - c_5$, and λ^*, the fiber distribution model was able to successfully represent the LCSL experimental results.

ate relationship when one structural parameter was based on confocal imaging ($R^2 = 0.62$ and 0.57; Fig. 10b–c), and had a strong relationship when two structural parameter values were based on confocal imaging ($R^2 = 0.97$; Fig. 10d). For each individual PAL experiment, the fiber distribution model using k and θ_p values based on confocal imaging predicted the stress response in four out of the eight specimens with moderately strong correlations to the experimental results ($R^2 > 0.5$; Table 3). In comparison, the fiber distribution model using k values from confocal imaging had fits with moderately strong correlations for three of the PAL specimens, the transversely isotropic model using θ_p values from confocal imaging had fits with moderately strong correlations for one PAL specimen, and the transversely isotropic model using no parameter values from confocal imaging had fits with moderately strong correlations for two PAL specimens (Table 3).

The fiber distribution model, using k and θ_p values from confocal imaging, predicted the PAL linear modulus and peak stress to within 20 and 10% of the average PAL experimental results, respectively (Table 4). When the fiber distribution model or transversely isotropic model used only one structural parameter value based on confocal imaging data, the linear modulus and peak stress were predicted within approximately 35–40% of the average PAL experimental results. The transversely isotropic model, using no structural parameter values from confocal imaging, significantly under predicted the PAL linear modulus and peak stress by 75 and 65% of the average PAL experimental results, respectively ($p < 0.05$).

4 Discussion

This study investigated whether differences in collagen fibril architecture at the microscale are predictive of differences in local mechanical behavior at the macroscale. By using confocal imaging and FFT, fibril dispersion and mean fibril orientation were quantified and input into constitutive models. This study found that incorporating specimen-specific structural parameters could improve model accuracy in predicting ligament mechanical behavior. These results support our hypothesis and emphasize the functional importance of collagen fibril architecture in ligament mechanics.

An important finding of this study is that the observed differences in the average mechanical behavior of two different ligaments (LCSL and PAL) were closely predicted by accounting for variations in the angular distribution of collagen fibrils (Fig. 10). When the stress response of ligament with a disorganized fibril network (PAL transverse) was modeled using the same model equations and parameters that provided an excellent fit to ligament with an aligned fibril network (LCSL transverse), the predicted mechanical behavior had a very weak correlation to the average PAL experimental values ($R^2 = 0.12$). The R^2 value was improved to 0.62 and 0.57 when either mean fibril orientation θ_p or fibril dispersion was measured from confocal imaging of the PAL, respectively. This prediction was further improved to an R^2 value of 0.97 when both mean fibril orientation θ_p and fibril dispersion k were measured from confocal images of the PAL. The inclusion of both structural parameter values based on confocal imaging also reduced the error in predict-

Table 3 Average material coefficients used to model the stress response of LCSL and PAL specimens, and the corresponding R^2 values of the curve fits between individual experimental and model results. The LCSL experiments were used to curve fit the non-structural parameters, c_1-c_5, and λ^*, while the PAL experiments were used to validate the stress response predicted by the model

Model type	Specimen type	c_1 (MPa)	c_2 (MPa)	c_3 (kPa)	c_4	c_5 (MPa)	Fibril dispersion k	Mean fibril orientation θ_p (deg)	Model fit to experimental data (R^2)
Trans iso (case 1)	LCSL long	2.0 ± 0.6	-2.0 ± 0.6	11.2 ± 10.8	67.4 ± 18.2	29.3 ± 15.8	500	0	1.00, 1.00, 1.00, 0.99, 0.99, 0.99, 0.98, 0.98
	LCSL trans	2.0 ± 0.6	-2.0 ± 0.6	11.2 ± 10.8	67.4 ± 18.2	29.3 ± 15.8	500	90	0.99, 0.99, 0.98, 0.98, 0.98, 0.98, 0.96, 0.93
	PAL trans	2.0 ± 0.6	-2.0 ± 0.6	11.2 ± 10.8	67.4 ± 18.2	29.3 ± 15.8	500	90	0.66, 0.51, 0.40, 0.01, -0.03, -0.05, -0.23, -0.48
Trans iso (case 2)	LCSL long	2.0 ± 0.6	-1.9 ± 0.6	11.4 ± 10.8	70.4 ± 17.4	32.2 ± 15.2	500	-1.3 ± 9.6	1.00, 1.00, 1.00, 0.99, 0.99, 0.99, 0.99, 0.98
	LCSL trans	2.0 ± 0.6	-1.9 ± 0.6	11.4 ± 10.8	70.4 ± 17.4	32.2 ± 15.2	500	88.7 ± 9.6	0.99, 0.99, 0.98, 0.98, 0.98, 0.98, 0.96, 0.93
	PAL trans	2.0 ± 0.6	-1.9 ± 0.6	11.4 ± 10.8	70.4 ± 17.4	32.2 ± 15.2	500	78.9 ± 39.3	0.66, 0.32, 0.22, 0.01, -0.03, -0.23, -0.48, -1.65
Fiber distr (case 3)	LCSL long	1.6 ± 1.0	-1.6 ± 1.0	16.1 ± 16.4	71.1 ± 17.3	40.7 ± 16.2	5.7 ± 5.3	0	1.00, 1.00, 1.00, 0.99, 0.99, 0.99, 0.99, 0.98
	LCSL trans	1.6 ± 1.0	-1.6 ± 1.0	16.1 ± 16.4	71.1 ± 17.3	40.7 ± 16.2	5.7 ± 5.3	90	0.99, 0.99, 0.98, 0.98, 0.98, 0.98, 0.96, 0.93
	PAL trans	1.6 ± 1.0	-1.6 ± 1.0	16.1 ± 16.4	71.1 ± 17.3	40.7 ± 16.2	1.1 ± 0.8	90	0.91, 0.63, 0.58, 0.45, 0.19, 0.15, -0.29, -2.22
Fiber distr (case 4)	LCSL long	1.6 ± 1.0	-1.5 ± 1.0	16.9 ± 16.8	71.9 ± 17.3	43.7 ± 15.7	5.7 ± 5.3	-1.3 ± 9.6	1.00, 1.00, 1.00, 0.99, 0.99, 0.99, 0.99, 0.98
	LCSL trans	1.6 ± 1.0	-1.5 ± 1.0	16.9 ± 16.8	71.9 ± 17.3	43.7 ± 15.7	5.7 ± 5.3	88.7 ± 9.6	0.99, 0.99, 0.98, 0.98, 0.97, 0.96, 0.93, 0.49
	PAL trans	1.6 ± 1.0	-1.5 ± 1.0	16.9 ± 16.8	71.9 ± 17.3	43.7 ± 15.7	1.1 ± 0.8	78.9 ± 39.3	0.92, 0.86, 0.69, 0.59, 0.22, -0.25, -3.81, -3.85

The average value used for λ^* was 1.050 ± 0.006 for all four models. All values in mean ± SD
LCSL-LG LCSL longitudinal, *LCSL-TR* LCSL transverse, *PAL-TR* PAL transverse

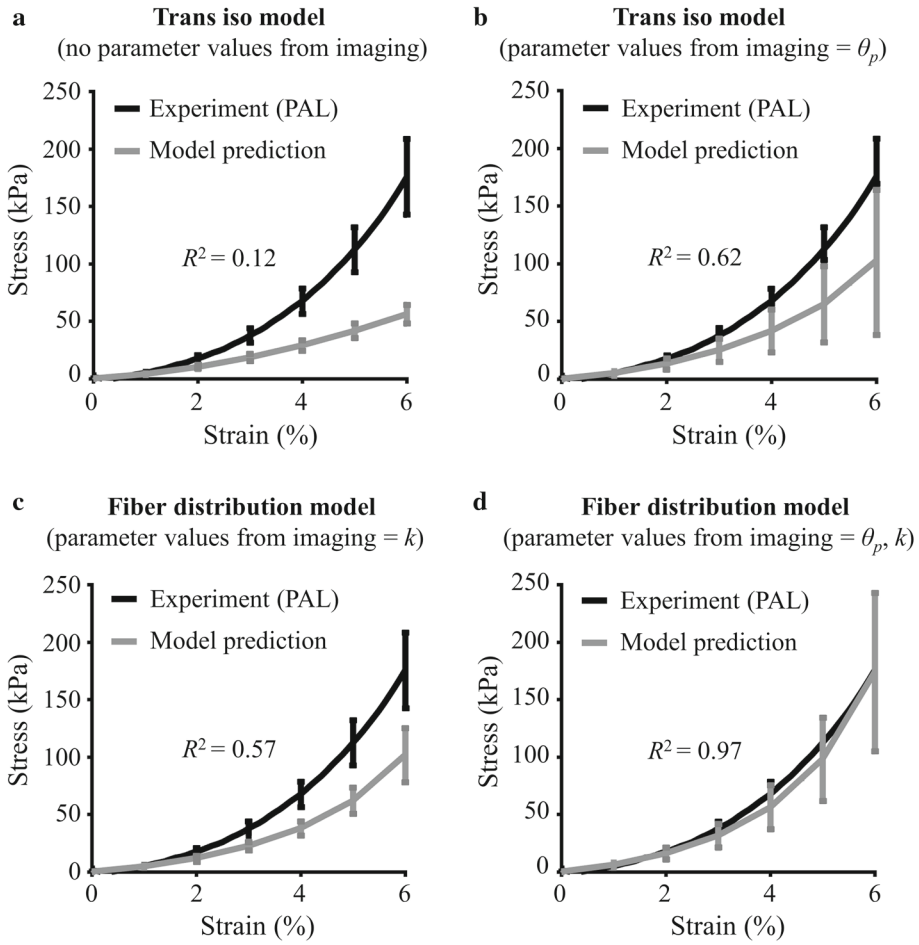

Fig. 10 Comparison between PAL transverse experimental data and model predictions. The following parameter values in the models were based on specimen-specific imaging data: **a** none, **b** mean fibril orientation θ_p, **c** fibril dispersion k, **d** mean fibril orientation θ_p and fibril dispersion k

Table 4 PAL mechanical properties from tensile experiments and model predictions

Type	Parameters from imaging	Linear region modulus (MPa)	Peak stress (kPa)
Experiment	–	5.6 ± 2.5	157.9 ± 60.1
Trans iso model	0	1.4 ± 0.4*	56.1 ± 16.5*
Trans iso model	1 (θ_p)	3.3 ± 5.1	101.7 ± 46.5
Fiber distr model	1 (k)	3.6 ± 2.2	96.3 ± 44.2
Fiber distr model	2 (θ_p, k)	6.7 ± 5.9	173.8 ± 137.2

Calculated at 6% grip-to-grip strain
*Significantly different between model prediction and experimental result ($p<0.05$); mean ± SD

ing the average PAL linear modulus and PAL peak stress by over three times. These results demonstrate that the predictive accuracy of the model is sensitive to both specimen-specific structural parameters, θ_p and k. Although the average fits were excellent when using θ_p and k from confocal imaging data, the fits of the individual PAL specimens were only moderately strong in half the specimens. The poor fits in half the PAL specimens explain the large standard deviations in the average PAL stress–strain predictions (Fig. 10d). When we examined microstructural differences between the PAL specimens with good and poor fits, we noticed that two of the PAL specimens with poor fits had fibril dispersion values similar to the paired LCSL, while all PAL specimens with good fits had at least half the fibril dispersion value relative to the paired LCSL. This suggests that either our modeling approach is not able to predict mechanical differences between specimens with similar fibril distributions, or the imaging and modeling methodology used in this study was unable to accurately represent the fibril network in all specimens. It is possible that predictions would be improved by imaging collagen networks at a higher scale with histology or polarized light imaging (Ni Annaidh et al. 2012), or by incorporating non-affine fibril kinematics and representative specimen geometry.

To our knowledge, this is the first study to use specimen-specific imaging data of collagen networks to model ligament, and it is one of the first research projects to use mechanical testing and imaging data of collagen fibrils to analyze the validity of a structural model of fibrous soft tissue. Most previously published research that uses fiber distribution models to predict soft tissue mechanics have estimated fiber parameters by using numerical methods. For example, several studies have used numerical methods to select a fiber dispersion parameter that optimized the model predictions to experimental results (Billiar and Sacks 2000; Driessen et al. 2005; Girard MJa, Downs JC, Bottlang M, Burgoyne CF, Suh J-KF, 2009; Hansen et al. 2009). The current study builds upon this prior work by directly measuring fiber parameters from specimens that were subjected to mechanical testing and inputting these measured structural parameters into the model. At least two other research projects used a similar experimental approach, as Wan et al. measured fiber orientation distribution of mouse carotid arteries using multiphoton microscopy (2012), and Szczesny et al. measured fiber orientation distribution of supraspinatus tendon using polarized light imaging (2012). Wan et al. and Szczesny et al. then incorporated the measured parameters into structural constitutive models. An important difference between these two prior research projects and the current study is that while the prior research used measured structural parameters to predict differences in mechanical response when individual specimens were subjected to different loading regimes, the current study used measured structural parameters to predict differences in mechanical response between specimens that were subjected to the same loading regime but were harvested from different anatomical locations (i.e., the LCSL and PAL). The one previous study we found that tested the predictive ability of a fiber distribution model to predict differences in tensile mechanics between specimens harvested at different anatomical locations was used for the dermis and had excellent fits, but only used a sample size of one for model predictions (Ni Annaidh et al. 2012). A rationale for our research design was that it could add to the existing knowledge by directly determining if the measured structural parameters could provide any predictive benefit when modeling tissues that have different fibrillar architecture, and thereby could give insight into the interrelations between macroscopic mechanical behavior and collagen fibril organization.

Findings from this study may help partially explain the inhomogeneity in mechanical behavior that has been observed in ligament and tendon. Previous studies found that the linear modulus from different regions of human ligament had an average coefficient of variation of 87% (Lujan et al. 2007, 2009), and from different regions of human supraspinatus tendon had a coefficient of variation of roughly 90% (Lake et al. 2009). These results are comparable to the current study, where the linear modulus from transverse tensile tests from two different regions (PAL and LCSL) had a coefficient of variation of 78%. Interestingly, we found that the large variation in LCSL and PAL mechanical behavior could be reasonably predicted by only accounting for regional differences in fibril dispersion and mean fibril ori-

entation. This is consistent with work by Lake et al. and Szczesny et al. that found a strong correlation between the linear modulus of supraspinatus tendon and the dispersion of the collagen fiber network (Lake et al. 2009; Szczesny et al. 2012). These results suggest that variability in mechanical behavior within a ligament is governed by the angular distribution of the collagen network. These findings are relevant to ongoing investigations into the microstructural origins of mechanical behavior in soft connective tissue (Fessel and Snedeker 2009; Henninger et al. 2013).

A potential application of the fiber distribution model is to describe and predict the functional impact of collagen remodeling in ligament and tendon. Growth and remodeling algorithms have been used to model many mechanobiological phenomena, including vascular growth (Hariton et al. 2007), bone remodeling (Cowin and Hegedus 1976), and tendon healing (Bajuri et al. 2016). During wound repair in ligament, the extracellular matrix reorganizes from a highly disperse and disorganized network of collagen to a network with moderate collagen alignment (Frank 2004). The fiber distribution model from this study has potential to predict the impact of these observed microstructural adaptations on the mechanical integrity of the damaged tissue. This could provide insight into remodeling behavior that is associated with robust ligament healing as well as recurrent sprains. This potential application is supported by a recent paper by Bajuri et al. 2016, which demonstrated that the fiber-reinforced hyperelastic models developed by Gasser et al. (2006) and Holzapfel et al. (2000) can successfully capture the mechanical behavior of the Achilles tendon at discrete time points during the healing process by adjusting the coefficient for fiber dispersion. Although the Bajuri et al. study did not use specimen-specific imaging data, it does suggest that collagen fiber alignment can be predictive of mechanical behavior in healing soft tissue.

A novel methodology was used in this study for parameter estimation. The material coefficients for the fiber distribution model were fit to experimental data from uniaxial tensile tests that were transverse and longitudinal to the visible fascicle orientation. Due to the inclusion of the von Mises distribution P in the strain energy formulation, the fiber network will actively resist deformation during both longitudinal and transverse loading. Therefore, we could not use previously established fitting methods for fiber-reinforced ligament models (Quapp and Weiss 1998), since the ground substance coefficients could not be fit to the transverse tests without also considering the stress contribution from the fiber network. An iterative automated method was applied that used an initial guess to first fit ground substance coefficients, $c_1 - c_{2,}$ to the transverse experimental data, and then updated this initial guess based on fitting the fiber network coefficients, $c_3 - c_5$, to the longitudinal experimental data. This method was successful, as we obtained excellent fits, regardless of whether zero, one or two structural coefficients, k and θ_p, were acquired from confocal imaging (Table 3). This method differs from previous research, which fit the non-structural parameters of fiber distribution models to just one set of experimental data (e.g., tensile tests longitudinal to the mean fiber direction) (Ni Annaidh et al. 2012).

The experimental and computational results from this study were compared to previously published data. For mechanical testing, the average linear modulus of 5.6 MPa from PAL transverse tests in this study was within the 1-15 MPa previously reported for bovine periodontal ligament (Pini et al. 2002), and the average linear modulus of 27.6 MPa from LCSL longitudinal tests in this study was very close to the 27 MPa reported for the calf patellar ligament (Eleswarapu et al. 2011). For constitutive modeling, the material coefficients calculated to best fit the transversely isotropic fiber model to the LCSL experimental data were compared to the material coefficients calculated in an earlier study by Quapp and Weiss (c_1-c_5 and λ^*; Table 3) (1998). There were no significant differences in the coefficients that represented ground substance, c_1-c_2, but significant differences ($p<0.05$) did exist in the material coefficients associated with the fibrous network, c_3 and c_5. These differences correspond to the lower linear modulus and peak stress observed in the bovine ligament experiments relative to human ligament.

Limitations exist in this study. The confocal microscopy technique used to autofluoresce collagen networks also autofluoresced elastin networks. Although elastin constitutes less than 5% of the total dry-weight of ligament (Gentleman et al. 2003), elastin still likely influenced the calculation of θ_p and k, and this should be considered when interpreting the results. Another limitation is that the structural parameters for each specimen were approximated from three confocal images that were each nearly 150 times smaller in area than the mechanically tested tissue. A sample size of three per specimen was determined acceptable because increasing the number of confocal images to seven per specimen only nominally changed the specimen's average microstructural parameters in a pilot study (data not shown). The structural parameters used in the constitutive models were only related to the two-dimensional collagen fiber distribution that we measured when the specimen was stretched into the linear region of the stress–strain curve, and we did not consider the load-dependent realignment of the collagen network (Lake et al. 2009), nor did we consider other structural parameters that have been shown to influence mechanical behavior, including the diameter, type, density, and interactions of collagen. Model predictions could potentially be improved by using a three-dimensional von Mises distribution, or including strain energy terms that model different fibrous networks (e.g., type I and type III collagen, elastin) and interactions between the fibrous networks and ground substance (Wag-

ner and Lotz 2004). In addition, this study only examined ligaments in neighboring regions of the bovine fetlock joint, and future work would need to determine if the measured fibril parameters can also improve model predictions in human ligaments from more diverse anatomical regions. Our results are based on a single volumetric element that did not account for specimen geometry or local strain behavior. Nevertheless, single elements can provide useful insight into fiber–matrix behavior (Fan and Sacks 2014), and grip-to-grip strain is a common measure to quantify the mechanical behavior of soft tissues (Henninger et al. 2013; Park and Ateshian 2006). Furthermore, grip-to-grip strain has a nearly linear correlation to midsubstance tissue strain (Peloquin et al. 2016; Tian et al. 2015) and has been previously used to model experimental data (Park and Ateshian 2006). Finally, this study tested the quasi-static mechanical behavior of ligament, and the strain-rate-dependent behavior of ligament was not accounted for within the constitutive equations.

In conclusion, this study used a structural constitutive model with confocal imaging data to determine that collagen fibril dispersion and mean fibril orientation were predictive of observed differences in ligament mechanical behavior. The primary function of ligament is mechanical; therefore, these results emphasize the importance of collagen fibril alignment on ligament function. Future work will use the fiber distribution model used in this study to investigate ligament remodeling and growth during normal and pathological processes. The findings of this study progress the structure–function knowledge of ligament and are applicable to the engineering and evaluation of functional replacement tissue.

Acknowledgements Research reported in this publication was supported by the General Medical Sciences of the National Institutes of Health under Award Numbers P20GM109095 and P20GM103408. We also acknowledge support from the Biomolecular Research Center at Boise State with funding from the National Science Foundation, Grants No. 0619793 and 0923535; the MJ Murdock Charitable Trust; and the Idaho State Board of Education. Kind thanks to Dr. Hazel Screen, Phil Boysen, and Carly Frank.

Compliance with ethical standards

Funding: This study was funded by the National Institute of General Medical Sciences (P20GM109095 and P20GM103408).

Conflicts of interest: The authors declare that they have no conflict of interest.

References

ASTM D3039 (2004) Standard test method for tensile properties of polymer matrix composite materials american society for testing and materials

Bajuri M, Isaksson H, Eliasson P, Thompson M (2016) A hyperelastic fibre-reinforced continuum model of healing tendons with distributed collagen fibre orientations. Biomech Model Mechanobiol 15:1457–1466. https://doi.org/10.1007/s10237-016-0774-5

Billiar KL, Sacks MS (2000) Biaxial mechanical properties of the native and glutaraldehyde-treated aortic valve cusp: part II–a structural constitutive model. J Biomech Eng 122:327–335. https://doi.org/10.1115/1.1287158

Clark J, Harryman D (1992) Tendons, ligaments, and capsule of the rotator cuff. Gross and microscopic anatomy. J Bone Joint Surg Am 74:713–725

Cowin S, Hegedus D (1976) Bone remodeling I: theory of adaptive elasticity. J Elast 6:313–326. https://doi.org/10.1007/BF00041724

Driessen N, Bouten C, Baaijens F (2005) A structural constitutive model for collagenous cardiovascular tissues incorporating the angular fiber distribution. J Biomech Eng-T ASME 127:494–503. https://doi.org/10.1115/1.1894373

Eleswarapu SV, Responte DJ, Athanasiou KA (2011) Tensile properties, collagen content, and crosslinks in connective tissues of the immature knee joint. PLoS ONE 6. https://doi.org/10.1371/journal.pone.0026178

Fan R, Sacks MS (2014) Simulation of planar soft tissues using a structural constitutive model: finite element implementation and validation. J Biomech 47:2043–2054. https://doi.org/10.1016/j.jbiomech.2014.03.014

Fessel G, Snedeker JG (2009) Evidence against proteoglycan mediated collagen fibril load transmission and dynamic viscoelasticity in tendon. Matrix Biol 28:503–510. https://doi.org/10.1016/j.matbio.2009.08.002

Frank C, Hart D, Shrive N (1999) Molecular biology and biomechanics of normal and healing ligaments—a review. Osteoarthr Cartil 7:130–140. https://doi.org/10.1053/joca.1998.0168

Frank CB (2004) Ligament structure physiology and function. J Musculoskelet Neuronal Interact 4:199–201

Freed AD, Einstein DR, Vesely I (2005) Invariant formulation for dispersed transverse isotropy in aortic heart valves: an efficient means for modeling fiber splay. Biomech Model Mechanobiol 4:100–117. https://doi.org/10.1007/s10237-005-0069-8

Gardiner JC, Weiss JA (2003) Subject-specific finite element analysis of the human medial collateral ligament during valgus knee loading. J Orthop Res 21:1098–1106. https://doi.org/10.1016/S0736-0266(03)00113-X

Gasser TC, Ogden RW, Ga Holzapfel (2006) Hyperelastic modelling of arterial layers with distributed collagen fibre orientations. J R Soc Interface 3:15–35. https://doi.org/10.1098/rsif.2005.0073

Gentleman E, Lay AN, Da Dickerson, Ea Nauman, Ga Livesay, Dee KC (2003) Mechanical characterization of collagen fibers and scaffolds for tissue engineering. Biomaterials 24:3805–3813. https://doi.org/10.1016/S0142-9612(03)00206-0

Girard MJa, Downs JC, Bottlang M, Burgoyne CF, Suh J-KF, (2009a) Peripapillary and posterior scleral mechanics–part II: experimental and inverse finite element characterization. J Biomech Eng, 131. https://doi.org/10.1115/1.3113683

Girard MJa, Downs JC, Burgoyne CF, Suh J-KF, (2009b) Peripapillary and posterior scleral mechanics-part I: development of an anisotropic hyperelastic constitutive model. J Biomech Eng -T AMSE, 131: https://doi.org/10.1115/1.3113682

Gohkle F, Essigkrug B, Schmitz F (1994) The pattern of the collagen fiber bundles of the capsule of the glenohumeral joint. J Shoulder and Elb Surg 3:111–128. https://doi.org/10.1016/S1058-2746(09)80090-6

Hansen L, Wan W, Gleason RL (2009) Microstructurally motivated constitutive modeling of mouse arteries cultured under altered axial stretch. J Biomech Eng, 131: https://doi.org/10.1115/1.3207013

Hariton I, deBotton G, Gasser T, Holzapfel G (2007) Stress-driven collagen fiber remodeling in arterial walls. Biomechan Model Mechanobiol 6:163–175. https://doi.org/10.1007/s10237-006-0049-7

Henninger HB, Underwood CJ, Romney SJ, Davis GL, Weiss JA (2013) Effect of elastin digestion on the quasi-static tensile response of medial collateral ligament. J Orthop Res 31:1226–1233. https://doi.org/10.1002/jor.22352

Holzapfel GA, Gasser TC, Ogden RAYW (2000) A new constitutive framework for arterial wall mechanics and a comparative study of material models. J Elast 61:1–48. https://doi.org/10.1023/A:1010835316564

Kastelic J, Galesklt A, Baer E (1978) The multicomposite structure of tendon. Connect Tissue Res 6:11–23. https://doi.org/10.3109/03008207809152283

Lake SP, Miller KS, Elliott DM, Soslowsky LJ (2009) Effect of fiber distribution and realignment on the nonlinear and inhomogeneous mechanical properties of human supraspinatus tendon under longitudinal tensile loading. J Orthop Res, 27: https://doi.org/10.1002/jor.20938

Lanir Y (1983) Constitutive equations for fibrous connective tissues. J Biomech 16:1–12. https://doi.org/10.1016/0021-9290(83)90041-6

Lujan TJ, Underwood CJ, Henninger HB, Thompson BM, Weiss JA (2007) Effect of dermatan sulfate glycosaminoglycans on the quasi-static material properties of the human medial collateral ligament. J Orthop Res 11:1–10. https://doi.org/10.1002/jor.20351

Lujan TJ, Underwood CJ, Jacobs NT, Ja Weiss (2009) Contribution of glycosaminoglycans to viscoelastic tensile behavior of human ligament. J Appl Physiol 106:423–431. https://doi.org/10.1152/japplphysiol.90748.2008

Maas S, BJ E, GA A, JA W, (2012) FEBio: finite elements for biomechanics. J Biomech Eng, 134. https://doi.org/10.1115/1.4005694

Mardia KV, Jupp PE (2000) Directional statistics. John Wiley & Sons Ltd, New York

Monici M (2005) Cell and tissue autofluorescence research and diagnostic applications. Biotechnol Ann Rev 11:227–256

Mooney M (1940) A theory of large elastic deformation. J Appl Phys, 11. https://doi.org/10.1063/1.1712836

Morrill E, Tulepbergenov A, Stender C, Lamichhane R, Brown R, Lujan T (2016) A software application for accurate quantification of fiber orientation distribution in soft tissue. Biomech Model Mechanobiol 15:1467–1478. https://doi.org/10.1007/s10237-016-0776-3

Ni Annaidh A, Bruyere K, Destrade M, Gilchrist MD, Maurini C, Ottenio M, Saccomandi G (2012) Automated estimation of collagen fibre dispersion in the dermis and its contribution to the anisotropic behaviour of skin. Ann Biomed Eng 40:1666–1678. https://doi.org/10.1007/s10439-012-0542-3

Park S, Ateshian GA (2006) Dynamic response of immature bovine articular cartilage in tension and compression, and nonlinear viscoelastic modeling of the tensile response. J Biomech Eng 128:623–630. https://doi.org/10.1115/1.2206201

Peloquin JM, Santare MH, Elliott DM (2016) Advances in quantification of meniscus tensile mechanics including nonlinearity. Yield, and Fail J Biomech Eng 138:021002. https://doi.org/10.1115/1.4032354

Pini M, Hwa W, Ss S, Botsis J, Mechanical BUC (2002) Mechanical characterization of bovine periodontal ligament. J Periodontal Res 37:237–244. https://doi.org/10.1034/j.1600-0765.2002.00344.x

Provenzano PP, Vanderby R (2006) Collagen fibril morphology and organization: implications for force transmission in ligament and tendon. Matrix Biol 25:71–84. https://doi.org/10.1016/j.matbio.2005.09.005

Quapp KM, Weiss JA (1998) Material characterization of human medial collateral ligament. J Biomech Eng T ASME 120:757–763. https://doi.org/10.1115/1.2834890

Rivlin R (1948) Large elastic deformations of isotropic materials. The R Soc, 241. https://doi.org/10.1098/rsta.1948.0024

Sacks MS (2003) Incorporation of experimentally-derived fiber orientation into a structural constitutive model for planar collagenous tissues. J Biomech Eng 125:280–287. https://doi.org/10.1115/1.1544508

Screen HRC, Lee DA, Bader DL, Shelton JC (2004) An investigation into the effects of the hierarchical structure of tendon fascicles on micromechanical properties. Proc Inst Mech Eng 218:109–119. https://doi.org/10.1243/095441104322984004

Szczesny S, Peloquin J, Cortes D, Kadlowec J, Soslowsky L, Elliott D (2012) Biaxial tensile testing and constitutive modeling of human supraspinatus tendon. J Biomech Eng, 134. https://doi.org/10.1115/1.4005852

Tian L, Henningsen J, Salick MR, Crone WC, Gunderson M, Dailey SH, Chesler NC (2015) Stretch calculated from grip distance accurately approximates mid-specimen stretch in large elastic arteries in uniaxial tensile tests. J Mech Behav Biomed Mater 47:107–113. https://doi.org/10.1016/j.jmbbm.2015.03.016

Wagner DR, Lotz JC (2004) Theoretical model and experimental results for the nonlinear elastic behavior of human annulus fibrosus. J Orthop Res 22:901–909. https://doi.org/10.1016/j.orthres.2003.12.012

Wan W, Dixon JB, Gleason RL (2012) Constitutive modeling of mouse carotid arteries using experimentally measured microstructural parameters. Biophys J 102:2916–2925. https://doi.org/10.1016/j.bpj.2012.04.035

Weiss JA, Maker BN, Govindjee S (1996) Finite element implementation of incompressible, transversely isotropic hyperelasticity. Comput Methods Appl Mech Eng 135:107–128